Quasi 1D Oxides as Electrocatalysts for Water-Splitting: Case study of $Sr_9M_2Mn_5O_{21}$ (M = Co, Ni, Cu, Zn)

Narayan Acharya[a], Surendra B. Karki[a], Farshid Ramezanipour[a,]*

[a]Department of Chemistry, University of Louisville, Louisville, Kentucky 40292, USA
*Corresponding author. Email: farshid.ramezanipour@louisville.edu, Phone: +1(502) 852-7061
ORCID: 0000-0003-4176-1386

Abstract

We have demonstrated that multi-metal oxides with quasi-1D structure can be effective electrocatalysts for water electrolysis. Four materials have been systematically investigated, namely $Sr_9Co_2Mn_5O_{21}$, $Sr_9Ni_2Mn_5O_{21}$, $Sr_9Cu_2Mn_5O_{21}$, and $Sr_9Zn_2Mn_5O_{21}$, comprising 1D chains of face-sharing MnO_6 octahedra and MO_6 trigonal prisms (M = Co, Ni, Cu or Zn), which are held together by strontium ions located between the chains. These materials show a consistent trend in electrocatalytic properties for both half-reactions of water-splitting, i.e., oxygen-evolution and hydrogen evolutions reactions (OER and HER). In particular, $Sr_9Ni_2Mn_5O_{21}$ has an outstanding performance for OER, with overpotential of 0.37 V, which is lower than those of many 3D and 2D oxides, and rivals the activity of noble metal catalysts, such as RuO_2. This is important given that OER is the considered the bottleneck of water-slitting process. Chronopotentiometry studies, combined with X-ray photoelectron spectroscopy (XPS) and X-ray diffraction experiments pre- and post-reaction, indicate that $Sr_9Ni_2Mn_5O_{21}$ is highly stable and retains its structural integrity upon electrocatalytic reactions. This study highlights the potential of quasi-1D oxides as active electrocatalysts for water-splitting.

1. Introduction

Many of the processes in renewable energy technologies require high-performing catalysts. In particular, catalysts comprising earth-abundant elements are of high importance. Electrocatalytic splitting of water, which is a promising method of green hydrogen production, requires active catalysts to make the process economical. The reaction consists of two components, namely the anodic oxygen-evolution reaction (OER) and the cathodic hydrogen-evolution reaction (HER). A major limitation of these reactions is their sluggish kinetics, which is often addressed using catalysts that contain costly noble metals, such as platinum, ruthenium, and iridium. It is essential to find alternative earth-abundant catalysts, particularly for OER, which is more energetically demanding. Transition metal oxides can be efficient and economic candidates as catalysts. Oxides with different structures have been explored for OER[1-3] and HER[4-6] electrocatalysis. They have mostly consisted of 3D oxides, such as perovskites,[1-7] but some quasi 2D oxides have also been explored.[8-10] In the latter case, the quasi 2D materials consisted of layers of six-coordinated transition metals, forming isolated stacks that are held together by lanthanide or alkaline-earth cations. Our research group has recently studied a wide range of oxide systems for electrocatalytic water-splitting.[11-15] Among various oxides, materials with 1D connectivity in their crystal structure, which are capable of water-splitting electrocatalysis, are rare. Even more scarce are 1D oxides that can catalyze both half reactions of water-splitting. One rare example is the quasi-1D system $Ca_2Sr_2Mn_2CoO_{10-\delta}$, showing good electrocatalytic activity for water-splitting, as described recently by our research group.[16] In this work, we investigate four quasi-1D transition metal oxides, and demonstrate their electrocatalytic performance. For the four materials studied in this work, the crystal structures of $Sr_9Co_2Mn_5O_{21}$[17] and $Sr_9Ni_2Mn_5O_{21}$[18] have been reported, both forming a trigonal *R*-3*c* structure, although the metal valence states were not determined. On the other hand, $Sr_9Cu_2Mn_5O_{21}$ and $Sr_9Zn_2Mn_5O_{21}$ have not been reported before. In this study, we have investigated the electrocatalytic properties of these four materials for both anodic and cathodic half-reactions of water-splitting.

2. Experimental

Synthesis and Characterization. Polycrystalline sample of $Sr_9Co_2Mn_5O_{21}$, $Sr_9Ni_2Mn_5O_{21}$, $Sr_9Cu_2Mn_5O_{21}$, and $Sr_9Zn_2Mn_5O_{21}$ were synthesized by solid-state synthesis method. Stoichiometric amounts of $SrCO_3$, MnO_2, Co_3O_4, NiO, CuO, and ZnO were mixed, pelletized, and heated in air at 1200°C for 24 h and then quenched in the air. This process was repeated four times, with re-grinding and re-palletization between heating cycles. The ramp rate of the furnace for heating and cooling was 100°C/h. Powder X-ray diffraction data were collected at room temperature using $CuK\alpha_1$ radiation (λ=1.54056 Å). The X-ray diffraction data were analyzed using GSAS[19] software with EXPEGUI interface.[20] X-ray photoelectron spectroscopy (XPS) was carried out using Al Kα radiation at room temperature. The microstructures were characterized using a Thermo Fisher Apreo C LoVac Field Emission Scanning Electron Microscope (SEM) with a Back-scattered detector (BSD) at an acceleration voltage of 5-30 kV.

Electrochemical Measurements. Electrochemical experiments were carried out in a three-electrode system using a rotating disk electrode at room temperature in 1 M KOH solution. A glassy carbon electrode loaded with the catalyst was used as the working electrode. Platinum (for OER) and carbon (for HER) were used as counter electrodes, and Hg/HgO was the reference electrode. The catalyst ink was prepared by mixing 35 mg of oxide catalyst, 7 mg of carbon black, 20 µl of nafion, and 7 ml of tetrahydrofuran (THF). The mixture was sonicated for 1 hour to get a homogeneous ink suspension in a 20 ml glass vial. The working electrode was prepared by dropcasting 20 µl (two coats of 10 µl) of the ink on a glassy carbon electrode. The electrochemical experiments were carried out using a rotating disc electrode at a rotation rate of 1600 rpm. The reference electrode was calibrated periodically using H_2 gas. The AC impedance method was used to measure resistance, which was then used for iR correction of potentials. The iR-corrected potentials were converted to the reversible hydrogen electrode (RHE) potential scale for all cyclic voltammograms (CVs). The conversion from Hg/HgO reference electrode scale to the RHE scale was done using the equation[21] $E_{\mathrm{RHE}} = E_{\mathrm{Hg/HgO}} + 0.0592\mathrm{pH} + E^{\circ}_{\mathrm{Hg/HgO}}$, where $E^{\circ}_{\mathrm{Hg/HgO}} = 0.098$ V. Chronopotentiometry experiments were done using two nickel foam electrodes, on which the catalyst ink had been dropcast. A current density of 10 $\mathrm{mA/cm^2}$ was applied and the potential was measured over time.

3. Results and Discussion

3.1. Crystal Structure

We note that the 1D connectivity in these materials only applies to the MnO_6/MO_6 polyhedra (M = Co, Ni, Cu or Zn), which form 1D chains. As mentioned previously, the crystal structures of $Sr_9Co_2Mn_5O_{21}$[17] and $Sr_9Ni_2Mn_5O_{21}$[18] have been reported to form a trigonal *R*-3*c* structure, although the metal valence states were not determined. On the other hand, $Sr_9Cu_2Mn_5O_{21}$ and $Sr_9Zn_2Mn_5O_{21}$ have not been reported before. We have found that these two new materials also form the same structure, with nearly identical X-ray diffraction patterns, as shown in Figure S1. The four materials belong to a family of oxides, where the general formula is often represented as $(A_3B_3O_9)_m(A_3MBO_6)_n$.[17, 18] For materials studied in this work, m = 1, n = 2, B = Mn, and B = Co, Ni, Cu or Zn. The $A_3B_3O_9$ building blocks contain three BO_6 octahedra (indicated by *a* in Figure 1), while the A_3MBO_6 component consists of two BO_6 octahedra located between two MO_6

trigonal prisms (*b* in Figure 1). These units are connected to form infinite chains of face-sharing MnO_6 octahedra (O), and MO_6 trigonal prisms (TP), which repeat in the sequence …-3O-TP-2O-TP-… (Figure 1).[17] This is expected given the ratio Mn/M = 5/2, and the longer bonds in trigonal prismatic coordination, which is more suitable for the large divalent M metals. The chains are held together by strontium ions, which reside between the chains and have alternating nine and ten-fold coordinations.

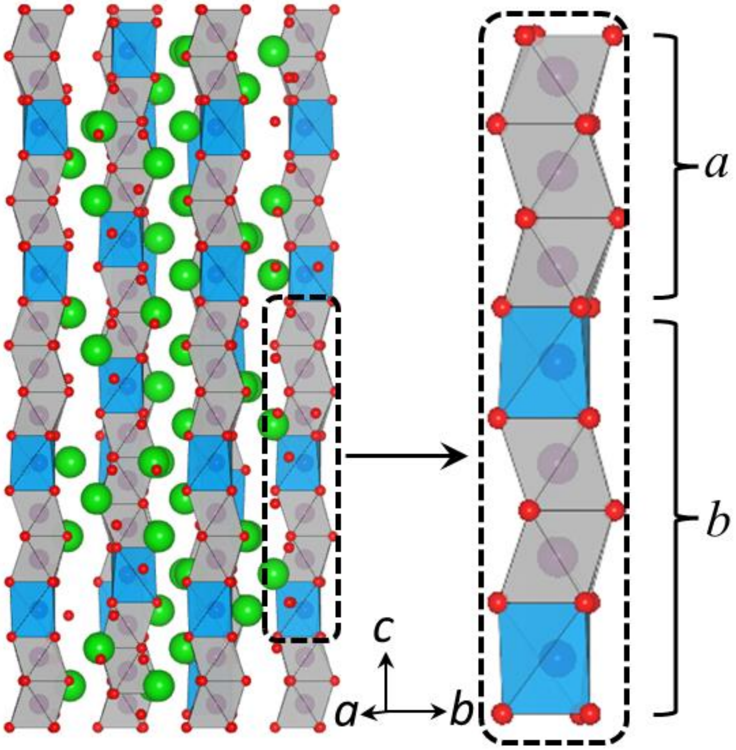

Figure 1. Crystal structure of $Sr_9M_2Mn_5O_{21}$ (M = Co, Ni, Cu, Zn). The MnO_6 and MO_6 polyhedra are shown in gray and blue, respectively. Green spheres represent strontium.

In terms of microstructure, these materials have similar grain sizes, as evident from the scanning electron microscopy (SEM) images in Figure S2. In addition, iodometric titrations were done for all four materials to determine the oxygen stoichiometry, showing 21 oxygens per formula unit. This was also confirmed by XPS, as described below.

3.2. X-ray Photoelectron Spectroscopy (XPS) Studies

The XPS spectra for manganese are shown in Figure 2. We note that the synthesis precursor for all materials contained tetravalent manganese, and the syntheses were done in air. Therefore, these materials are expected to contain tetravalent manganese. The binding energies for different valence states of manganese in oxides are close to each other. Therefore, we also obtained XPS spectra on reference materials, Mn_2O_3 and MnO_2, for comparison. As shown in Figure 2, the manganese spectra for all four materials are consistent with tetravalent state, showing binding energies above 642 eV.[22-24]

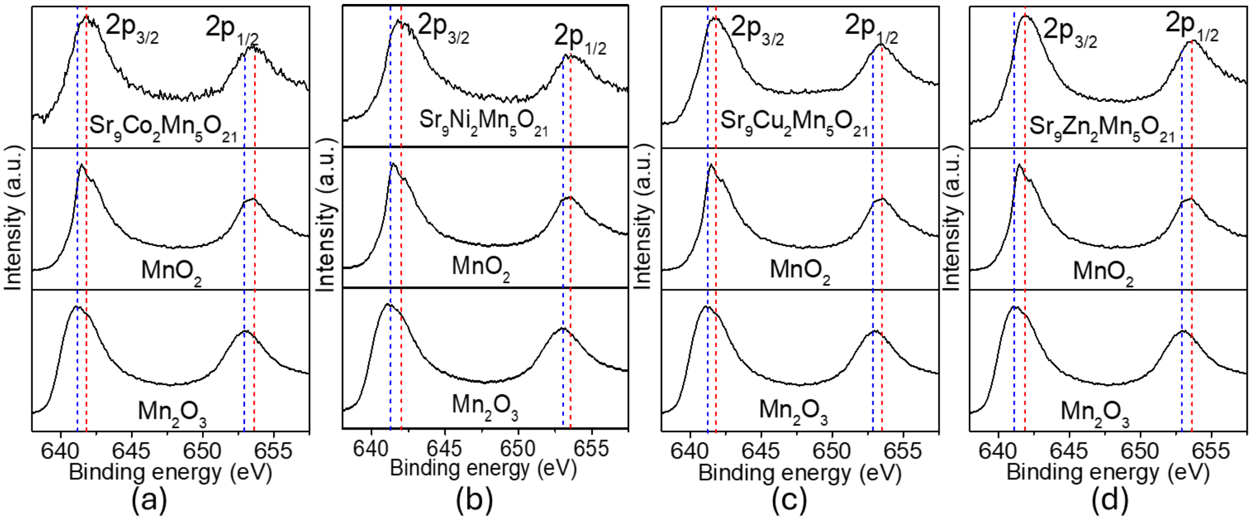

Figure 2. XPS spectra showing tetravalent manganese for all four materials: (a) $Sr_9Co_2Mn_5O_{21}$, (b) $Sr_9Ni_2Mn_5O_{21}$, (c) $Sr_9Cu_2Mn_5O_{21}$, and (d) $Sr_9Zn_2Mn_5O_{21}$. The Mn_2O_3 and MnO_2 spectra are also shown for comparison.

For $Sr_9Co_2Mn_5O_{21}$, the cobalt spectrum (Figure 3a) shows the $2p_{3/2}$ peak at about 780 eV, along with a satellite peak at about 786 eV. The $2p_{3/2}$ and satellite peak positions are consistent with divalent cobalt.[25, 26] We note that the satellite for trivalent cobalt would appear at about 9-10 eV higher than the $2p_{3/2}$ peak,[27] which is not observed here. Therefore, the XPS spectrum indicates that cobalt is in divalent state. For $Sr_9Ni_2Mn_5O_{21}$, the $2p_{3/2}$ peak for Ni^{2+} is expected to appear in the range of ~854 eV[22, 28, 29] to ~855.1 eV.[30] The nickel spectrum in Figure 3b shows the $2p_{3/2}$ peak at about 855.06 eV, indicating divalent nickel. For $Sr_9Cu_2Mn_5O_{21}$, the copper spectrum (Figure 3c) shows the $2p_{3/2}$ peak at about 933.8 eV, along with satellite peaks at 940.8 eV and 943.4 eV. These are consistent with divalent copper, as expected.[22] For $Sr_9Zn_2Mn_5O_{21}$, the zinc spectrum (Figure 3d) shows the $2p_{3/2}$ peak at about 1021.2 eV as expected for divalent zinc.[31]

Therefore, the XPS studies indicate that all four materials comprise tetravalent manganese combined with divalent cobalt, nickel, copper or zinc.

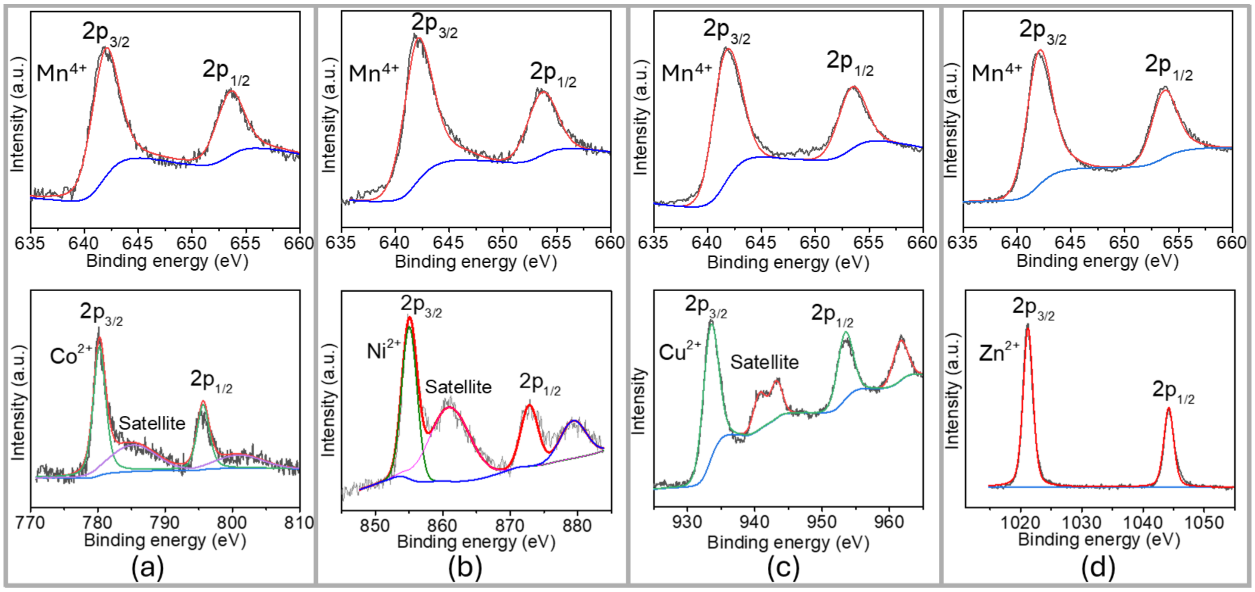

Figure 3. XPS spectra for (a) $Sr_9Co_2Mn_5O_{21}$, (b) $Sr_9Ni_2Mn_5O_{21}$, (c) $Sr_9Cu_2Mn_5O_{21}$, and (d) $Sr_9Zn_2Mn_5O_{21}$, showing divalent cobalt, nickel, copper and zinc, respectively. Manganese is tetravalent in all four materials.

3.2. Electrocatalytic Properties for HER

The electrocatalytic activities of the four materials were first investigated for the cathodic reaction of water-sitting, i.e., hydrogen-evolution reaction (HER). Figure 4a shows the polarization curves for the four materials. The onset potential, where a sudden increase in the current-response signifies the start of the HER, is one of the parameters used for the evaluation of different electrocatalysts. However, there are often uncertainties in choosing the onset potential by different observers.[32] Therefore, by convention, the overpotential at 10 mA/cm^2 is used for comparison of different HER electrocatalysts.

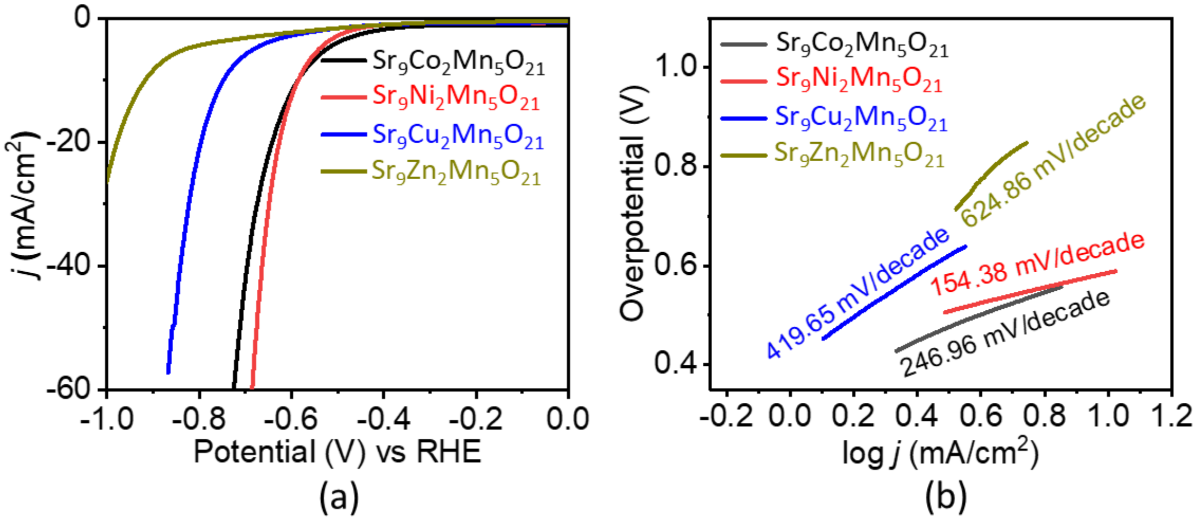

Figure 4. (a) HER polarization curves in 1M KOH. (b) HER Tafel plots and slopes.

The overpotential is the excess potential beyond the thermodynamic value, which is required to operate an electrocatalytic reaction.[21, 33, 34] The thermodynamic potential for HER is 0 V vs RHE. The overpotential values at 10mA/cm^2 for $Sr_9Co_2Mn_5O_{21}$, $Sr_9Ni_2Mn_5O_{21}$, $Sr_9Cu_2Mn_5O_{21}$, and $Sr_9Zn_2Mn_5O_{21}$ are -0.58 V, -0.58 V, -0.75 V, and -0.92 V, respectively. Clearly, the Co and Ni-containing materials show the lowest overpotentials. The overpotentials of these materials are not as low as those of some oxides such as $LaFeO_3$ (-0.48 V)[35] and $Ca_2FeCoO_{6-\delta}$ (-0.25 V),[13] but are lower than those reported for some others, such as $Ca_2Sr_2Mn_2FeO_{10-\delta}$ (-0.66 V) and $LaSr_2Fe_3O_8$ (-0.77 V).[36] The HER kinetics was evaluated using the Tafel equation, which is expressed as $\eta = a + b\log j$,[37] where $a = -(2.303RT/\alpha F)\log j_0$, $b = 2.303RT/\alpha F$, η is overpotential, j_0 is exchange current density, α is charge transfer coefficient, T is temperature, F is Faraday constant, R is universal gas constant, and j is the current density.[37] Faster HER kinetics is marked by a smaller slope of the plot of η versus log$j$. As seen in Figure 4b, the lowest Tafel slopes are observed for $Sr_9Ni_2Mn_5O_{21}$

and $Sr_9Co_2Mn_5O_{21}$, which also show the lowest overpotentials, indicating better electrocatalytic activity.

3.3. Electrocatalytic Properties for OER

The electrocatalytic activities of all four materials were also investigated for the anodic reaction of water-sitting, i.e., oxygen-evolution reaction (OER), which is usually considered the bottleneck for the water-sitting process. Figure 5a shows the OER polarization curves, indicating that $Sr_9Ni_2Mn_5O_{21}$ has the lowest onset potential. Also, this material shows the lowest overpotential, defined as $\eta_{10} = E - 1.23$ V, where 1.23 V is the thermodynamic OER potential, and E is the potential at 10 mA/cm^2.

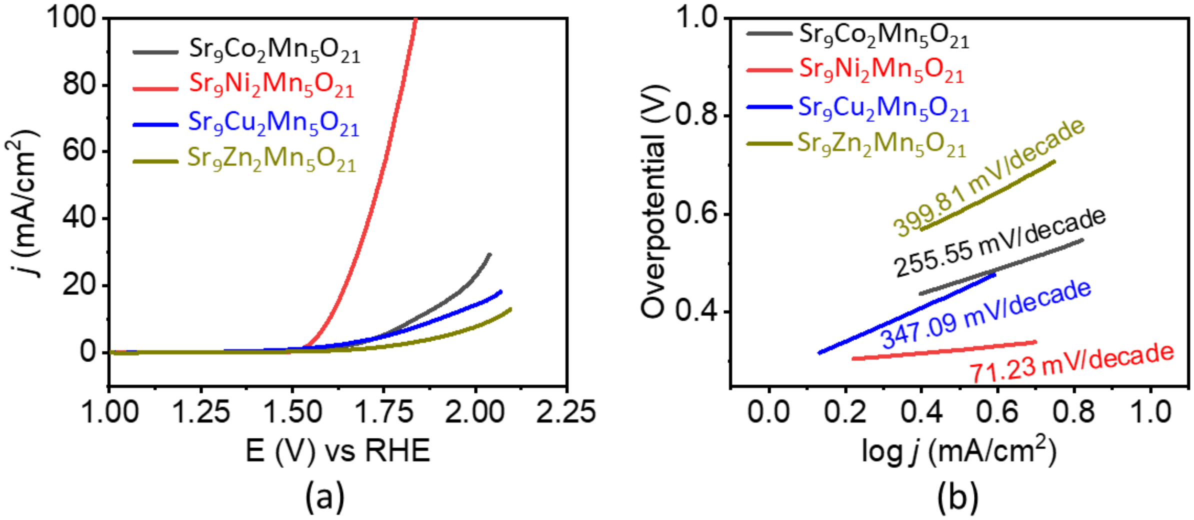

Figure 5. (a) OER polarization curves in 1M KOH. (b) OER Tafel plots and slopes.

The overpotential values are η_{10} = 0.61 V, 0.37 V, 0.67 V, and 0.82 V for $Sr_9Co_2Mn_5O_{21}$, $Sr_9Ni_2Mn_5O_{21}$, $Sr_9Cu_2Mn_5O_{21}$, and $Sr_9Zn_2Mn_5O_{21}$, respectively. The OER activity of $Sr_9Ni_2Mn_5O_{21}$ is remarkable, and its overpotential is comparable to that of the noble metal catalyst RuO_2, with a reported overpotential of ~0.4 V in 1 M KOH.[38] It is also lower than those reported for many other oxide catalysts, such as $NdBaMn_2O_{5.5}$ (~0.4 V),[34] $LaSr_2Fe_3O_8$ (0.63 V),[36]

$LaMn_{0.5}Co_{0.5}O_3$ (0.46 V),[11] and $LaFeO_3$ (0. 47 V).[35] In addition, it leads to the fastest OER kinetics, as indicated by the Tafel plots in Figure 5b, which show the lowest Tafel slope for $Sr_9Ni_2Mn_5O_{21}$. In addition, chronopotentiometry experiments were done to demonstrate the stability of this catalyst, as shown in Figure S3, which indicates excellent stability for 100 hours.

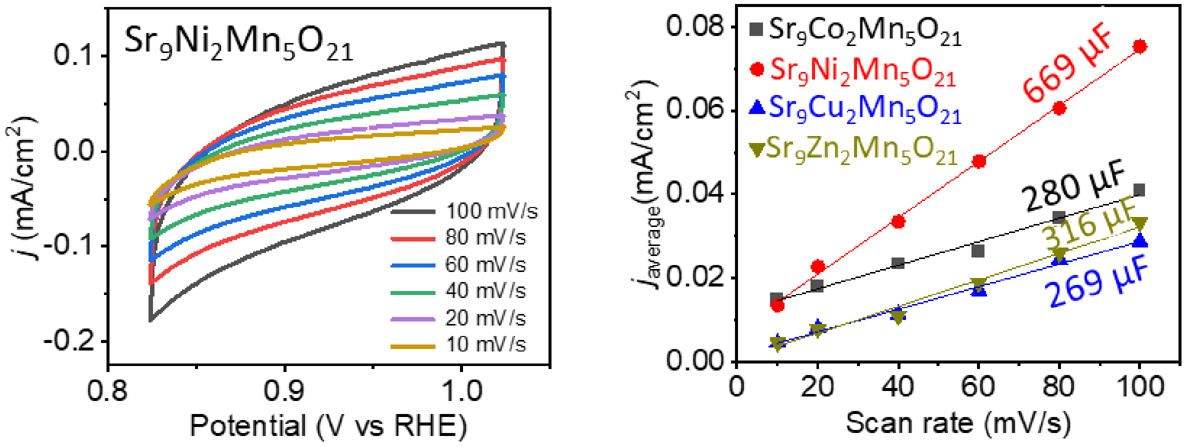

(a) (b)

Figure 6. (a) Representative cyclic voltammetry data for $Sr_9Ni_2Mn_5O_{21}$ in non-faradaic potential region. (b) Plots of $j_{average}$ versus scan rate, indicating the double layer capacitance (C_{dl}) as slope.

We also evaluated the double-layer capacitance (C_{dl}), which is important due to its direct proportionality to the electrochemically active surface area.[39] This is done by cyclic voltammetry experiments at different scan rates in a non-faradaic potential region, where electron transfer processes are insignificant. The C_{dl} value can be obtained using the equation[39] $j_{average} = C_{dl}\, v$. In this equation, $j_{average}$ is the average of the absolute values of j_{anodic} and $j_{cathodic}$ at the middle potential of the non-Faradaic CV, and ν is the scan rate. Therefore, the C_{dl} value can be obtained from the slope of the $j_{average}$ versus v plot.[39] As observed in Figure 6, the best catalyst, $Sr_9Ni_2Mn_5O_{21}$, also shows the highest C_{dl} value among the four materials. Furthermore, we obtained electrochemical impedance spectroscopy (EIS) data for all four materials under OER conditions, indicating the lower charge transfer resistance of $Sr_9Ni_2Mn_5O_{21}$ compared to the other three materials, as shown in Figure S5.

We also evaluated the stability of the best catalyst, $Sr_9Ni_2Mn_5O_{21}$, by XPS and X-ray diffraction before and after electrocatalytic OER experiments, as shown in Figure 7. The X-ray diffraction pattern of $Sr_9Ni_2Mn_5O_{21}$ remains nearly unchanged after OER, indicating that this material retains its structural framework upon electrocatalytic activity. In addition, we were interested in confirming whether manganese, which has multiple stable oxidation states, and can be prone to oxidation, retains its valence state in $Sr_9Ni_2Mn_5O_{21}$. The XPS spectra in Figure 7b show almost no change in binding energies of $2p_{3/2}$ and $2p_{1/2}$ peaks, confirming the stability of $Sr_9Ni_2Mn_5O_{21}$.

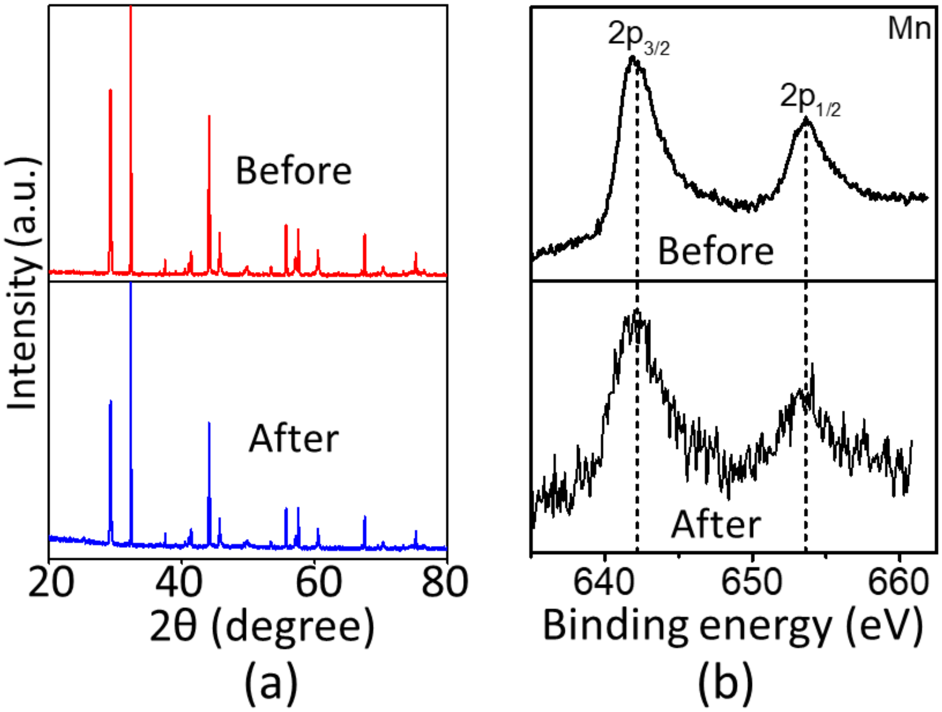

Figure 7. (a) X-ray diffraction data and (b) XPS spectra showing the Mn peaks, before and after OER experiments for $Sr_9Ni_2Mn_5O_{21}$.

The enhanced electrocatalytic activity of $Sr_9Ni_2Mn_5O_{21}$ is related to the unique characteristics of nickel in this compound. Nickel-based oxides have shown interesting catalytic activities for different electrochemical reactions.[40, 41] The ability of Nickel to undergo reversible changes in valence state, from −1 to +4, is a contributing factor.[40-42] Among the materials studied in this work, the incorporation of cobalt, nickel, copper and zinc lead to a wide range of electrocatalytic performances, with the nickel-containing material showing the best performance. This may be in part related to the higher electronegativity of nickel.[43] It has been suggested that higher electronegativity of the transition metal leads to a better hybridization of metal 3d and oxygen 2p states, which enhances the electrocatalytic activity.[44] We note that copper has a similar electronegativity to nickel.[43] However, compared to nickel, copper shows a lower degree of versatility in its valence states, which is essential to the electron transfer processes involved in electrocatalytic reactions. The importance of the ability to acquire different valence states to the capability of undergoing various electronic transitions in OER/HER electrocatalysis has been discussed before.[41,42] Therefore, we attribute the higher electrocatalytic activity of the Ni-containing material to a combination of higher electronegativity and versatile valence states of nickel, which reenforce each other's effects.

4. Conclusions

Overall, the remarkable electrocatalytic performance, high stability, and the ability to catalyze both half-reactions of water-splitting are outstanding features that indicate quasi-1D oxides can be suitable candidates for applications as electrocatalysts in water electrolysis. In particular the OER activity of $Sr_9Ni_2Mn_5O_{21}$ surpasses those of many previously reported 3D and 2D oxides, and is comparable to that of noble metal catalysts such as RuO_2. Thus, this work introduces a new family of highly active oxide electrocatalysts, featuring a quasi-1D structure, for electrochemical water-splitting.

Supporting Information: X-ray diffraction data, structural parameters, SEM images, chronopotentiometry data, cyclic voltammetry data in non-faradaic region, electrochemical impedance spectroscopy data in the OER potential region.

Acknowledgment. This work is supported by the National Science Foundation (NSF) under grant no. DMR-1943085.

Conflict of Interests. Authors declare no conflict of interests.

References

1. Suntivich, J.; May, K. J.; Gasteiger, H. A.; Goodenough, J. B.; Shao-Horn, Y., A Perovskite Oxide Optimized for Oxygen Evolution Catalysis from Molecular Orbital Principles. *Science* **2011,** *334* (6061), 1383-1385.
2. Zhu, Y.; Zhou, W.; Chen, Z.-G.; Chen, Y.; Su, C.; Tadé, M. O.; Shao, Z., $SrNb_{0.1}Co_{0.7}Fe_{0.2}O_{3-\delta}$ Perovskite as a Next-Generation Electrocatalyst for Oxygen Evolution in Alkaline Solution. *Angew. Chem., Int. Ed. Engl.* **2015,** *54* (13), 3897-3901.
3. Su, C.; Wang, W.; Chen, Y.; Yang, G.; Xu, X.; Tadé, M. O.; Shao, Z., $SrCo_{0.9}Ti_{0.1}O_{3-\delta}$ As a New Electrocatalyst for the Oxygen Evolution Reaction in Alkaline Electrolyte with Stable Performance. *ACS Appl. Mater. Interfaces* . **2015,** *7* (32), 17663-17670.
4. Karki, S. B.; Ramezanipour, F., Pseudocapacitive Energy Storage and Electrocatalytic Hydrogen-Evolution Activity of Defect-Ordered Perovskites $Sr_xCa_{3-x}GaMn_2O_8$ (x = 0 and 1). *ACS Appl. Energy Mater.* **2020,** *3*, 10983-10992.
5. Tian, S.; He, J.; Huang, H.; Song, T.-s.; Wu, X.; Xie, J.; Zhou, W., Perovskite-Based Multifunctional Cathode with Simultaneous Supplementation of Substrates and Electrons for Enhanced Microbial Electrosynthesis of Organics. *ACS Appl. Mater. Interfaces* **2020,** *12* (27), 30449-30456.
6. Hona, R. K.; Karki, S. B.; Ramezanipour, F., Oxide Electrocatalysts Based on Earth-Abundant Metals for Both Hydrogen- and Oxygen-Evolution Reactions. *ACS Sustain. Chem. Eng.* **2020,** *8*, 11549-11557.
7. Alom, M. S.; Kananke-Gamage, C. C. W.; Ramezanipour, F., Perovskite Oxides as Electrocatalysts for Hydrogen Evolution Reaction. *ACS Omega* **2022,** *7*, 7444-7451.
8. Liu, S.; Sun, C.; Chen, J.; Xiao, J.; Luo, J.-L., A High-Performance Ruddlesden–Popper Perovskite for Bifunctional Oxygen Electrocatalysis. *ACS Catal.* **2020,** *10*, 13437-13444.
9. Forslund, R. P.; Hardin, W. G.; Rong, X.; Abakumov, A. M.; Filimonov, D.; Alexander, C. T.; Mefford, J. T.; Iyer, H.; Kolpak, A. M.; Johnston, K. P.; Stevenson, K. J., Exceptional electrocatalytic oxygen evolution via tunable charge transfer interactions in $La_{0.5}Sr_{1.5}Ni_{1-x}Fe_xO_{4\pm\delta}$ Ruddlesden-Popper oxides. *Nat. Commun.* **2018,** *9*, 3150.
10. Xiao, H.; Liu, P.; Wang, W.; Ran, R.; Zhou, W.; Shao, Z., Ruddlesden–Popper Perovskite Oxides for Photocatalysis-Based Water Splitting and Wastewater Treatment. *Energy Fuels* **2020,** *34* (8), 9208-9221.
11. Alom, M. S.; Ramezanipour, F., Vacancy effect on the electrocatalytic activity of $LaMn_{1/2}Co_{1/2}O_{3-\delta}$ for hydrogen and oxygen evolution reactions. *Chem. Commun.* **2023,** *59*, 5870-5873.
12. Hona, R. K.; Ramezanipour, F., Remarkable Oxygen-Evolution Activity of a Perovskite Oxide from the $Ca_{2-x}Sr_xFe_2O_{6-\delta}$ Series. *Angew. Chem.* **2019,** *58*, 2060-2063.
13. Karki, S. B.; Hona, R. K.; Yu, M.; Ramezanipour, F., Enhancement of Electrocatalytic Activity as a Function of Structural Order in Perovskite Oxides. *ACS Catal.* **2022,** *12*, 10333-10337.
14. Hona, R. K.; Karki, S. B.; Cao, T.; Mishra, R.; Sterbinsky, G. E.; Ramezanipour, F., Sustainable Oxide Electrocatalyst for Hydrogen- and Oxygen-Evolution Reactions. *ACS Catal.* **2021,** *11*, 14605-14614.
15. Acharya, N.; Karki, S. B.; Giordano, L.; Ramezanipour, F., A Design Strategy for Highly Active Oxide Electrocatalysts by Incorporation of Oxygen-Vacancies. *Small* **2024**, 2403415.

16. Karki, S. B.; Hona, R. K.; Ramezanipour, F., Electrocatalytic activity and structural transformation of $Ca_2Sr_2Mn_2MO_{10-\delta}$ (M = Fe, Co). *Ionics* **2022,** *28* (1), 397-406.

17. Boulahya, K.; Parras, M.; González-Calbet, J. M.; Martínez, J. L., Structural−Magnetic Properties Relationship in a New Commensurate Material: $Sr_9Mn_5Co_2O_{21}$. *Chem. Mater.* **2004,** *16* (25), 5408-5413.

18. Hernando, M.; Boulahya, K.; Parras, M.; González-Calbet, Jose M.; Amador, U., Synthesis and Microstructural Characterisation of Two New One-Dimensional Members of the $(A_3NiMnO_6)_\alpha(A_3Mn_3O_9)_\beta$ Homologous Series (A = Ba, Sr). *Eur. J. Inorg. Chem.* **2003,** *2003* (13), 2419-2425.

19. Larson, A. C.; Von Dreele, R. B., *General Structure Analysis System (GSAS), Los Alamos National Laboratory Report LAUR* **2004**, 86-748.

20. Toby, B., EXPGUI, a graphical user interface for GSAS. *J. Appl. Cryst.* **2001,** *34*, 210-213.

21. Kawashima, K.; Márquez, R. A.; Son, Y. J.; Guo, C.; Vaidyula, R. R.; Smith, L. A.; Chukwuneke, C. E.; Mullins, C. B., Accurate Potentials of Hg/HgO Electrodes: Practical Parameters for Reporting Alkaline Water Electrolysis Overpotentials. *ACS Catal.* **2023,** *13* (3), 1893-1898.

22. Moulder, J. F.; Stickle, W. F.; Sobol, P. E.; Bomben, K. D.; editor Chastain, J., **1992,** *Handbook of X-ray photoelectron spectroscopy: a reference book of standard spectra for identification and interpretation of XPS data.*, Perkin-Elmer, Eden Prairie.

23. Chen, Z.; Wang, J.; Chao, D.; Baikie, T.; Bai, L.; Chen, S.; Zhao, Y.; Sum, T. C.; Lin, J.; Shen, Z., Hierarchical Porous $LiNi_{1/3}Co_{1/3}Mn_{1/3}O_2$ Nano-/Micro Spherical Cathode Material: Minimized Cation Mixing and Improved Li+ Mobility for Enhanced Electrochemical Performance. *Sci. Rep.* **2016,** *6*, 25771.

24. Pandey, D. K.; Modi, A.; Gaur, N., Revealing the structural and magnetic susceptibility aspects of Sr^{2+} substituted $Y_{2-x}Sr_xNiMnO_6$ ($0\leq x\leq 0.1$) compounds. *J. Appl. Phys.* **2019,** *126*.

25. Jena, A.; Penki, T. R.; Munichandraiah, N.; Shivashankar, S. A., Flower-like porous cobalt(II) monoxide nanostructures as anode material for Li-ion batteries. *J. Electroanal. Chem.* **2016,** *761*, 21-27.

26. Chuang, T. J.; Brundle, C. R.; Rice, D. W., Interpretation of the x-ray photoemission spectra of cobalt oxides and cobalt oxide surfaces. *Surf. Sci.* **1976,** *59*, 413-429.

27. Dupin, J. C.; Gonbeau, D.; Benqlilou-Moudden, H.; Vinatier, P.; Levasseur, A., XPS analysis of new lithium cobalt oxide thin-films before and after lithium deintercalation. *Thin Solid Films* **2001,** *384*, 23-32.

28. Zhao, Q.; Fang, C.; Tie, F.; Luo, W.; Peng, Y.; Huang, F.; Ku, Z.; Cheng, Y.-B., Regulating the Ni^{3+}/Ni^{2+} ratio of NiOx by plasma treatment for fully vacuum-deposited perovskite solar cells. *Mater. Sci. Semicond. Process.* **2022,** *148*, 106839.

29. Fan, L.; Liu, P. F.; Yan, X.; Gu, L.; Yang, Z. Z.; Yang, H. G.; Qiu, S.; Yao, X., Atomically isolated nickel species anchored on graphitized carbon for efficient hydrogen evolution electrocatalysis. *Nat. Commun.* **2016,** *7*, 10667.

30. Cheng, M.; Fan, H.; Song, Y.; Cui, Y.; Wang, R., Interconnected hierarchical $NiCo_2O_4$ microspheres as high-performance electrode materials for supercapacitors. *Dalton Trans.* **2017,** *46*, 9201-9209.

31. Al-Gaashani, R.; Radiman, S.; Daud, A. R.; Tabet, N.; Al-Douri, Y., XPS and optical studies of different morphologies of ZnO nanostructures prepared by microwave methods. *Ceram. Int.* **2013,** *39*, 2283-2292.

32. Benck, J. D.; Hellstern, T. R.; Kibsgaard, J.; Chakthranont, P.; Jaramillo, T. F., Catalyzing the Hydrogen Evolution Reaction (HER) with Molybdenum Sulfide Nanomaterials. *ACS Catal.* **2014,** *4*, 3957-3971.

33. Lu, F.; Zhou, M.; Zhou, Y.; Zeng, X., First-Row Transition Metal Based Catalysts for the Oxygen Evolution Reaction under Alkaline Conditions: Basic Principles and Recent Advances. *"Small"* **2017,** *13* (45), 1701931.

34. Wang, J.; Gao, Y.; Chen, D.; Liu, J.; Zhang, Z.; Shao, Z.; Ciucci, F., Water Splitting with an Enhanced Bifunctional Double Perovskite. *ACS Catal.* **2018,** *8* (1), 364-371.

35. Dai, J.; Zhu, Y.; Zhong, Y.; Miao, J.; Lin, B.; Zhou, W.; Shao, Z., Enabling High and Stable Electrocatalytic Activity of Iron-Based Perovskite Oxides for Water Splitting by Combined Bulk Doping and Morphology Designing. *Adv. Mater. Interfaces* **2019,** *6* (1), 1801317.

36. Karki, S. B.; Andriotis, A. N.; Menon, M.; Ramezanipour, F., Bifunctional Water-Splitting Electrocatalysis Achieved by Defect Order in $LaA_2Fe_3O_8$ (A = Ca, Sr). *ACS Appl. Energy Mater.* **2021,** *4*, 12063-12066.

37. Fang, Y.-H.; Liu, Z.-P., Tafel Kinetics of Electrocatalytic Reactions: From Experiment to First-Principles. *ACS Catal.* **2014,** *4*, 4364-4376.

38. Das, D.; Das, A.; Reghunath, M.; Nanda, K. K., Phosphine-free avenue to Co_2P nanoparticle encapsulated N,P co-doped CNTs: a novel non-enzymatic glucose sensor and an efficient electrocatalyst for oxygen evolution reaction. *Green Chem.* **2017,** *19* (5), 1327-1335.

39. Connor, P.; Schuch, J.; Kaiser, B.; Jaegermann, W., The Determination of Electrochemical Active Surface Area and Specific Capacity Revisited for the System MnOx as an Oxygen Evolution Catalyst. *Z. fur Phys. Chem.'* **2020,** *234* (5), 979-994.

40. Han, L.; Dong, S.; Wang, E., Transition-Metal (Co, Ni, and Fe)-Based Electrocatalysts for the Water Oxidation Reaction. *Adv Mater* **2016,** *28* (42), 9266-9291.

41. Vij, V.; Sultan, S.; Harzandi, A. M.; Meena, A.; Tiwari, J. N.; Lee, W.-G.; Yoon, T.; Kim, K. S., Nickel-Based Electrocatalysts for Energy-Related Applications: Oxygen Reduction, Oxygen Evolution, and Hydrogen Evolution Reactions. *ACS Catal.* **2017,** *7* (10), 7196-7225.

42. Angeles-Olvera, Z.; Crespo-Yapur, A.; Rodríguez, O.; Cholula-Díaz, J. L.; Martínez, L. M.; Videa, M., Nickel-Based Electrocatalysts for Water Electrolysis. *Energies* **2022,** *15* (5), 1609.

43. Little, E. J., Jr.; Jones, M. M., A complete table of electronegativities. *J. Chem. Educ.* **1960,** *37*, 231-233.

44. Suntivich, J.; Hong, W. T.; Lee, Y.-L.; Rondinelli, J. M.; Yang, W.; Goodenough, J. B.; Dabrowski, B.; Freeland, J. W.; Shao-Horn, Y., Estimating Hybridization of Transition Metal and Oxygen States in Perovskites from O K-edge X-ray Absorption Spectroscopy. *J. Phys. Chem. C* **2014,** *118*, 1856-1863.